



A positivity-preserving scheme for fluctuating hydrodynamics

Francesco Magaletti^{a,*}, Mirko Gallo^b, Sergio P. Perez^c, José A. Carrillo^d,
Serafim Kalliadas^c

^a Advanced Engineering Centre, School of Architecture, Technology and Engineering, University of Brighton, Lewes Road, Brighton BN2 4GJ, United Kingdom

^b Dipartimento di Ingegneria Meccanica e Aerospaziale, Università degli Studi di Roma La Sapienza, Via Eudossiana 18, Roma 00184, Italy

^c Department of Chemical Engineering, Imperial College London, London SW7 2AZ, United Kingdom

^d Mathematical Institute, University of Oxford, Woodstock Road, Oxford OX2 6GG, United Kingdom

ARTICLE INFO

Article history:

Received 2 November 2021

Received in revised form 31 March 2022

Accepted 19 April 2022

Available online 26 April 2022

Keywords:

Positivity-preserving hybrid numerical scheme

Fluctuating hydrodynamics

Diffuse interface

Stochastic partial differential equations

Two-phase flows

ABSTRACT

A finite-difference hybrid numerical method for the solution of the isothermal fluctuating hydrodynamic equations is proposed. The primary focus is to ensure the positivity-preserving property of the numerical scheme, which is critical for its functionality and reliability especially when simulating fluctuating vapour systems. Both cases of single- and two-phase flows are considered by exploiting the van der Waals' square-gradient approximation to model the fluid (often referred to as "diffuse-interface" model). The accuracy and robustness of the proposed scheme is verified against several benchmark theoretical predictions for the statistical properties of density, velocity fluctuations and liquid-vapour interface, including the static structure factor of the density field and the spectrum of the capillary waves excited by thermal fluctuations at interface. Finally, the hybrid scheme is applied to the challenging bubble nucleation process, and is shown to capture the salient features of the phenomenon, namely nucleation rate and subsequent bubble-growth dynamics.

© 2022 The Author(s). Published by Elsevier Inc. This is an open access article under the CC BY license (<http://creativecommons.org/licenses/by/4.0/>).

1. Introduction

Thermal fluctuations in fluids are ubiquitous in a wide spectrum of physical phenomena and technological applications. From activated processes such as bubble [1] and crystal nucleation [2] to thin-film [3], nano-thread instabilities [4], molecular motors [5] and biological systems such as lipid membranes [6] and Brownian engines [7]. Thermal fluctuations play a central role in these systems by enabling energy-barrier crossing transitions, which in applications, such as nucleation, cannot be modelled by deterministic mean-field approaches.

The dynamical evolution of systems with thermal fluctuations is often studied via microscopic simulations such as molecular dynamics (MD) or Monte Carlo (MC) methodologies, which naturally account for fluctuations. However, the enormous computational cost of having to resolve at least three degrees of freedom per particle, is a significant drawback of atomistic simulations, and despite drastic improvements in computational power, such simulations are still only applicable for small fluid volumes (typically few nm^3). Moreover, atomistic approaches rely on the use of a thermostat [8] or barostat [9] which can be a major additional challenge, not yet fully resolved. For instance, in the presence of non-uniform shear, a global

* Corresponding author.

E-mail address: f.magaletti@brighton.ac.uk (F. Magaletti).

thermostat such as Nosé-Hoover, can cause artificial effects, e.g. a non-uniform temperature distribution which in turn will set up thermally-driven motion of the particles.

More recently, continuum mechanics approaches embedding thermal fluctuations in the spirit of the Landau and Lifshitz's fluctuating hydrodynamics (FH) [10] have attracted increasing interest for their potential in exploring large domains, but also long timescales with respect to particle methods. Indeed, FH has already been applied to several systems. Fluid behaviour at the nanoscale including fluid-structure interactions [11] and ionic liquids [12], showing also good agreement with atomistic simulations [13], liquid-vapour systems [14], thermodiffusion in multi-component mixtures [15], homogeneous bubble nucleation [16,17] and boiling inception [18], are only a few applications of FH. However, the Landau and Lifshitz approach is mostly phenomenological and is not based on first principles: they intuitively added stochastic flux terms to the Navier-Stokes (NS) equations where dissipation is expected, i.e. in the stress tensor, leading to a set of stochastic partial differential equations (SPDEs). Not surprisingly, there have been several efforts to obtain first-principle derivations of FH. One of the most well-known works is that of Kawasaki [19] and Dean [20]. Starting from a system of non-interacting Langevin equations, they formally derived a stochastic equation for the microscopic density field of a system of non-interacting Brownian particles (with Dean's equation being the overdamped counterpart of the Kawasaki one). A formal derivation of the so-called Dean-Kawasaki (DK) model is given in Ref. [21] and a rigorous approach in Ref. [22].

Despite the considerable attention the DK model has received, it remains disconnected from the original Landau-Lifshitz formulation, and a common misconception in the literature is that it can be used to describe the evolution of macroscopic quantities. But in fact DK has never really left the Langevin realm. Hence there is a need to formalise the connection between DK and FH to enable the description of observable fields and remove the dependence on the (microscopic) Langevin equations. One way to do that is via dynamic density functional theory (DDFT), an extension of equilibrium statistical mechanics where the dynamic variation of a conserved variable is given by the gradient of a flux with an advective part proportional to the local flow velocity and a diffusive part proportional to the gradient of a free-energy functional. DDFT has gained much traction over the last few years with applications ranging from active media and crystallisation [2,23,24] to complex fluids and molecular self-assembly [25,26]. Rigorous derivations have been proposed for both overdamped and inertial regimes, accounting for additional effects such as hydrodynamic interactions and particle anisotropy-orientation [27–30]. A comprehensive review of DDFT is given in the recent article in Ref. [31]. In particular, a bottom-up systematic derivation of not only FH but also fluctuating DDFT (FDDFT) has been recently proposed in [32]: it provides a new first-principle formulation that includes thermal fluctuations on the (mean-field) DDFT. Such derivation stays in tune with the early intuitive FH from Landau and Lifshitz, and alleviates the misconception mentioned earlier.

Accounting for fluctuations in non-equilibrium processes is central to all these approaches. In FH, the noise term is classically based on the assumptions of Gaussianity and small intensity (i.e. $\sqrt{\langle \delta f^2 \rangle} / \langle f \rangle \ll 1$, with f the field under consideration) around equilibrium conditions. Under these hypotheses, Landau & Lifshitz [10] stipulated an expression for the stochastic force, \mathbf{f}_{st} , in terms of a zero-mean and delta-correlated symmetric-and-traceless-tensor white noise, $\boldsymbol{\eta}$,

$$\mathbf{f}_{\text{st}} = \nabla \cdot \tilde{\boldsymbol{\tau}} = \sqrt{2k_B T_{eq} \mu_{eq}} \boldsymbol{\eta} \quad (1)$$

where k_B , T_{eq} , and μ_{eq} are the Boltzmann constant, the equilibrium temperature of the system and the dynamic viscosity of the fluid at equilibrium, respectively. This expression was later derived by enforcing the fluctuation-dissipation balance (FDB) [33], after linearising the NS equations around an equilibrium state. The common approach in dealing with nonequilibrium conditions makes use of the assumption that the correlations of the fluctuating fields obey a local-equilibrium version of the FDB [34]. This local-equilibrium approximation (LEA) is the usual way to proceed in nonequilibrium thermodynamics [35], where the equilibrium laws, like the equation of state (EOS) expressing the pressure as a function of density and temperature, $p = p(\rho, T)$, continue to hold for the locally defined fluid properties, $p(\mathbf{x}, t) = p(\rho(\mathbf{x}, t), T(\mathbf{x}, t))$. It is worth noting that LEA is also involved in fundamental approaches like DDFT [36,37] (the essence of LEA in DDFT is the introduction of a frame of reference moving with the average velocity of the particles, so that in the moving frame the system appears at rest with each particle seeing all other particles as if at equilibrium [32]). Following the LEA, the stress-tensor correlation is obtained by substituting the local temperature, $T(\mathbf{x}, t)$, and viscosity, $\mu(\mathbf{x}, t)$, in Eq. (1). A more refined derivation, makes use of projection operator techniques [38]. However, it does not provide information about force moments higher than the second, and hence unable to resolve the much debated issue of the Gaussian nature of the noise. An even more robust approach, starts from first principles and makes use of the Fokker-Planck equation (FPE) for the distribution function of the hydrodynamics fields [39–41]. It enables to take into account both fluctuations and nonlinearities in non-equilibrium conditions. The connection with the corresponding Langevin equations for the hydrodynamic fields was later obtained in [42].

As already highlighted, the noise contribution is obtained by enforcing the FDB. This is crucial when devising numerical schemes for the solution of SPDEs: the FDB must be reproduced also at the discrete level. In other words, the functional properties of the derivative operators (such as gradient, divergence, and Laplacian) must also be reproduced by their discrete counterparts. For example, the identity $\nabla^\dagger = -\nabla$, stating that the adjoint of the gradient operator is equal to the negative divergence operator, must be guaranteed by the discrete versions of the gradient and divergence operators, \mathcal{G} and \mathcal{D} , respectively. Not surprisingly, the majority of previous research efforts have been dedicated to providing FDB-compliant algorithms. Finite-volume [43,44], finite-difference [45], and finite-element [46,47] approaches have been proposed. The performance of different time-integration schemes has been analysed in [48]. All these schemes faithfully reproduce the

statistical properties of the fluctuating fields. However, the stochastic forcing might cause unphysical negative densities or temperatures during the numerical evolution, causing blow-up of the solution [14]. This is particularly common when e.g. simulating rarefied vapour regions, or liquid-vapour systems at low temperatures. Adding to the numerical difficulties, overdamped formulations are more prone to suffering from negative densities, compared to inertial descriptions. This is because in the former case the noise is contained in the density equation, the only equation for the system, while in the latter case the noise is in the momentum equation (which is coupled to the density equation). In a recent work [49], a finite-volume scheme was developed to overcome the challenge of preserving non-negative densities in overdamped equations with noise. At the heart of the scheme is a Brownian bridge technique that halves the time step every time a negative density is encountered, guaranteeing that the correct Brownian path is followed by respecting the values of the normal distributions in Eq. (1).

The need for positivity-preserving schemes has naturally emerged in the context of compressible fluids, where maintaining accurate solutions of the Euler equations is a problem which is particularly acute for the case of rarefied vapours. Merely replacing the numerically negative density values by positive ones is not a remedy and does not enable stable numerical solutions, less alone accurate ones. As a consequence, accurate and robust positivity-preserving schemes have been developed, such as the first-order schemes in Refs. [50,51]. More recently, a general framework for constructing arbitrarily high-order positivity-preserving discontinuous Galerkin, finite-volume and finite-difference schemes for the solution of the Euler equations has been proposed [52–54]. The extension to the compressible NS equations has also been considered in [55].

The case of fluctuating conservation laws has not been considered as of yet. A notable exception, however, is our recent effort in Ref. [49], albeit with a simplified model, an overdamped FDDFT, where momentum is adiabatically slaved to density. The present study goes a step further than our previous article and formulates a positivity-preserving numerical scheme for FH, both in single and two-phase systems (liquid-vapour). The scheme warrants the positivity of the density field throughout the dynamic evolution in practical experiments without relying on the Brownian bridge concept [49]. Density positivity is a crucial feature especially when simulating multiphase flows, and phase transition processes. Specifically, our scheme is a hybrid one combining upwind and central discretisations to take advantage of both the positivity-preserving property of the former and the FDB-compliance of the latter. The accuracy and robustness of this hybrid approach is validated against several benchmark cases, including analytical predictions, both in single and two phase systems. The structure of the algorithm is relatively simple without requiring evaluation of complex flux limiters and as a result it is computationally cheap and efficient.

§ 2 is devoted to the model equations for fluctuating fluid systems in both single and two-phase conditions; § 3 details the formulation of the hybrid numerical scheme, providing also proofs for the positivity-preserving property on the density field; § 4 focuses on numerical applications of the proposed scheme and compares the results against classical approaches, such as fully-central or fully-upwind ones. Finally, § 5 offers conclusions and discussions of extensions.

2. Governing equations

As discussed in the Introduction, FH was first introduced by Landau & Lifshitz [10] to describe weak fluctuations in fluids, strictly speaking at equilibrium, but later was extended to address the more complex non-equilibrium conditions [41,42], even in two-phase systems [56,57]. In what follows, we retrieve the basic equations describing the evolution of the density and momentum fields, under the simplifying hypothesis of isothermal flows, i.e. considering the temperature as an externally assigned parameter.

The general fluctuating conservation laws for mass and momentum read:

$$\begin{aligned} \frac{\partial \rho}{\partial t} + \nabla \cdot (\rho \mathbf{u}) &= 0, \\ \frac{\partial \rho \mathbf{u}}{\partial t} + \nabla \cdot (\rho \mathbf{u} \otimes \mathbf{u}) &= \nabla \cdot \boldsymbol{\tau} + \nabla \cdot \tilde{\boldsymbol{\tau}}, \end{aligned} \quad (2)$$

with ρ the density, \mathbf{u} the fluid velocity, $\boldsymbol{\tau}$ the deterministic stress tensor, and $\tilde{\boldsymbol{\tau}}$ the stochastic stress tensor. The deterministic stress tensor depends on the functional form of the free energy and can be derived by applying classical non-equilibrium thermodynamic principles, in particular requiring a non-negative entropy production [35]. This also allows to clearly distinguish between the reversible and irreversible contributions to the stress tensor. A linear constitutive law for the irreversible contribution provides the classical NS viscous stress tensor:

$$\boldsymbol{\tau} = \boldsymbol{\tau}_{rev} + \boldsymbol{\tau}_{irr} = \boldsymbol{\tau}_{rev} + \mu \left(\nabla \mathbf{u} + \nabla \mathbf{u}^T - \frac{2}{3} \nabla \cdot \mathbf{u} \mathbf{I} \right), \quad (3)$$

with μ the dynamic viscosity. It should be noted that the functional form of the NS viscous contribution has a gradient-flow structure and is conservative (under divergence). This is in contrast with FDDFT where there is exchange of momentum between the fluid particles and an external bath resulting in a non-conservative noise contribution [32] (except for the overdamped limit where momentum is adiabatically slaved to density).

An appropriate equation of state (EoS) is used to reproduce the thermodynamic properties of the specific fluid. Usually, the EoS is given in terms of the local Helmholtz free energy $f(\rho, T)$, where T denotes the temperature. In the case of simple fluids

$$\boldsymbol{\tau}_{rev} = -p\mathbf{I}, \quad (4)$$

with the pressure $p = -\partial f / \partial v|_T = \rho^2 \partial f / \partial \rho|_T$.

To describe a two-phase liquid-vapour system, the hypothesis of a local free energy is no more sufficient. In the general DFT approach [58], the free energy is approximated as a non-local functional of the spatially-dependent fluid density (one-body position distribution), $F[\rho(\mathbf{x})]$. This functional, which typically consists of two parts, the free energy of an ideal fluid, F_{id} , and the excess-over-ideal free energy, enables to study structure in the fluid as well as global phase diagrams [59–63]. In this study, the van der Waals square-gradient approximation of the free-energy functional is adopted, often referred to as diffuse-interface (DI) model, which can be obtained from a truncated Taylor expansion of the DFT free-energy functional [64, 65]:

$$F[\rho, T] = \int_{\Omega} \left(\rho f(\rho, T) + \frac{\lambda}{2} |\nabla \rho|^2 \right) dV, \quad (5)$$

where the two terms, $\rho f(\rho, T)$ and $(\lambda/2)|\nabla \rho|^2$, ensure the existence of a well-defined interface, and the capillary coefficient λ is related to the interfacial properties of the liquid-vapour system, namely surface tension and interface thickness. More specifically, the value of λ can be tuned to reproduce the surface-tension of the specific fluid under investigation, with a constant value sufficient to reproduce the temperature dependence of surface tension [57].

By using elements from non-equilibrium thermodynamics [35], the following expression for the reversible contribution of the stress tensor is obtained:

$$\boldsymbol{\tau}_{rev} = \left(-p + \frac{\lambda}{2} |\nabla \rho|^2 + \lambda \rho \nabla^2 \rho \right) \mathbf{I} - \lambda \nabla \rho \otimes \nabla \rho, \quad (6)$$

the so-called Korteweg or capillary stress tensor for two-phase systems in the DI formulation, and comprising the effect of surface tension at the liquid-vapour interface. A detailed derivation of this object is provided in Appendix A for the reader's convenience. The deterministic constitutive law for the stress tensor of the two-phase system (Eqs. (3), (6)) can be also framed in the context of other non-equilibrium thermodynamics frameworks, i.e. *GENERIC* [66,67].

The DI model has been shown to be able to capture the rich hydrodynamics of multiphase systems and associated complex phenomena, such as phase transformation, latent heat release, shock emission, and topological changes [68–70]. The square-gradient approximation has also been used successfully to describe multiphase systems at different levels of complexity including phase change, contact-line dynamics-spreading of droplets [71,72] and boiling [73]. However, let us highlight that the cornerstone of all these approaches are transport equations which are phenomenological and they represent conservation statements for the mass, momentum and energy; on the other hand DDFT and FDDFT are based on first principles and are fundamental.

As already highlighted in the Introduction, in the Landau-Lifshitz approach, the stochastic terms follow from the FDB. As a consequence, they will only depend on the explicit form of the irreversible contributions to the stress tensor. After some algebra, the stochastic stress tensor is expressed in terms of a delta-correlated white noise symmetric tensor $\boldsymbol{\eta}(\mathbf{x}, t)$ with components

$$\tilde{\tau}_{ij} = \sqrt{2k_B T \mu} \left[\eta_{ij} - \delta_{ij} \frac{1}{3} \eta_{kk} \right], \quad (7)$$

with k_B the Boltzmann constant, δ_{ij} the Kronecker delta and with

$$\langle \eta_{ij}(\mathbf{x}, t) \rangle = 0, \quad (8)$$

$$\langle \eta_{ij}(\mathbf{x}, t) \eta_{i'j'}(\mathbf{x}', t') \rangle = (\delta_{ii'} \delta_{jj'} + \delta_{ji'} \delta_{ij'}) \delta(\mathbf{x} - \mathbf{x}') \delta(t - t') \quad (9)$$

(details of the derivation are given in [57]).

For the bulk free energy $f(\rho, T)$ we adopt the modified Benedict-Webb-Rubin EoS that reproduces well the thermodynamic properties of a Lennard-Jones (LJ) fluid [74]. Dimensionless variables are defined as $\rho^* = \rho/\rho_r$, $T^* = T/T_r$ by employing the parameters of the LJ potential as reference quantities, i.e. $\sigma = 3.4 \times 10^{-10}$ m as length, $\epsilon = 1.65 \times 10^{-21}$ J as energy, $m = 6.63 \times 10^{-26}$ kg as mass and $T_r = \epsilon/k_B$ as temperature. As a consequence, we have the following reference quantities for the density, velocity, time and pressure, respectively: $\rho_r = m/\sigma^3$, $V_r = \sqrt{\epsilon/m}$, $t_r = \sigma/V_r$ and $P_r = \epsilon/\sigma^3$. The non-dimensional capillary coefficient is chosen as $\lambda^* = \lambda m^2/(\sigma^5 \epsilon) = 5.224$ to reproduce LJ values in a wide range of temperatures. To account for the viscosity variability due to the liquid-vapour density contrast and temperature, $\mu^*(\rho^*, T^*)$, we chose the viscosity of an LJ fluid [75]. The dimensionless form of Eq. (2) finally reads

$$\begin{aligned}
\frac{\partial \rho^*}{\partial t^*} + \nabla^* \cdot (\rho^* \mathbf{u}^*) &= 0, \\
\frac{\partial \rho^* \mathbf{u}^*}{\partial t^*} + \nabla^* \cdot (\rho^* \mathbf{u}^* \otimes \mathbf{u}^*) &= \nabla^* \cdot \left[\left(-p^* + \frac{\lambda^*}{2} |\nabla^* \rho^*|^2 + \lambda^* \rho^* \nabla^{*2} \rho^* \right) \mathbf{I} - \lambda^* \nabla^* \rho^* \otimes \nabla^* \rho^* \right] \\
&\quad + \nabla^* \cdot \left[\mu^* \left(\nabla^* \mathbf{u}^* + \nabla^{*T} (\mathbf{u}^*) - \frac{2}{3} \nabla^* \cdot \mathbf{u}^* \mathbf{I} \right) \right] \\
&\quad + \nabla^* \cdot \left(\sqrt{2T^* \mu^* \bar{\eta}} \right),
\end{aligned} \tag{10}$$

where $\bar{\eta}$ is a non-dimensional symmetric, traceless and normal distributed noise tensor. For convenience, in what follows we drop the superstars.

3. Numerical method

Our numerical scheme is based on a finite-difference approximation on a staggered (or “MAC”) and uniform grid with spacing h . This means that scalar quantities are located at points (i, j, k) at the cell centre, while vectors are face-centred, placing the x -component at $(i + 1/2, j, k)$ points, the y -component at $(i, j + 1/2, k)$, and the z -component at $(i, j, k + 1/2)$.

The use of a centred discretisation might require a strong limitation on the timestep, Δt , in order to ensure the positivity of the density field. We provide a proof of this statement in the one-dimensional (1D) case by exploiting an explicit Euler temporal scheme. It is sufficient to look at the density equation, which is discretised as follows:

$$\rho_i^{n+1} = \rho_i^n - \frac{\Delta t}{h} \left(\rho u_{i+1/2}^n - \rho u_{i-1/2}^n \right), \tag{11}$$

where the superscript indicates the time instant and the subscript indicates the spatial location. It is evident that, given a positive density field at time t^n , a sufficient condition to keep positivity is

$$\Delta t < \frac{h \rho_i^n}{|\rho u_{i+1/2}^n - \rho u_{i-1/2}^n|} \leq \frac{h \min_i(\rho_i^n)}{\max_i(|\rho u_{i+1/2}^n - \rho u_{i-1/2}^n|)} \leq \frac{h \min_i(\rho_i^n)}{2 \max_i(|\rho u_{i+1/2}^n|)}, \tag{12}$$

where the presence of the minimum density value at the numerator generates a strong timestep limitation, especially in conditions with small vapour densities.

A much better control of the sign of the density field is enabled by upwind schemes – see [76,77] and the references therein for upwind schemes and density positivity. However, the use of a staggered grid requires a slight modification with respect to classical co-located upwind schemes. We use the velocity as a primary variable, instead of the momentum. As a result, the velocity components are naturally face-centred, while the momenta, $\hat{\mathbf{q}} = (\hat{q}_x, \hat{q}_y, \hat{q}_z)^T$, at the same locations, are reconstructed from the velocity and density values. In 1D, our scheme follows as

$$\rho_i^{n+1} = \rho_i^n - \frac{\Delta t}{h} \left(\hat{q}_{x i+1/2}^n - \hat{q}_{x i-1/2}^n \right). \tag{13}$$

Let us analyse now two different reconstructions, namely, a cell-centred reconstruction (CR) and a first order upwind reconstruction (UR):

$$\hat{q}_{x i+1/2}^{\text{CR}} = \frac{1}{2} u_{i+1/2} (\rho_i + \rho_{i+1}), \tag{14}$$

$$\hat{q}_{x i+1/2}^{\text{UR}} = \begin{cases} \rho_i u_{i+1/2}, & u_{i+1/2} \geq 0 \\ \rho_{i+1} u_{i+1/2}, & u_{i+1/2} < 0. \end{cases} \tag{15}$$

When Eq. (14) is applied to Eq. (13), the following centred scheme is obtained

$$\rho_i^{n+1} = \left[1 - \frac{\Delta t}{2h} (u_{i+1/2}^n - u_{i-1/2}^n) \right] \rho_i^n - \frac{\Delta t u_{i+1/2}^n}{2h} \rho_{i+1}^n + \frac{\Delta t u_{i-1/2}^n}{2h} \rho_{i-1}^n, \tag{16}$$

where the value of the density at the next timestep is expressed as a linear combination of previous values. A convex combination of previous density values would guarantee the sign of the density to remain positive throughout the evolution. However, in Eq. (16) the sign of the coefficients in the linear combination is controlled by the (unknown) sign of the velocities $(u_{i+1/2}^n, u_{i-1/2}^n)$, hence a convex combination is not *a-priori* granted, and positivity-preserving is not ensured. This is especially apparent for the coefficients in front of ρ_{i+1}^n and ρ_{i-1}^n . On the contrary, a convex combination with all positive coefficients, hence preserving positivity, occurs when we make use of Eq. (15), $\hat{q} = \hat{q}^{\text{UR}}$. This is proven for the case of positive velocities, but all the other cases follow straightforwardly. Under the hypothesis of velocity being positive, Eq. (13) is rewritten as

$$\rho_i^{n+1} = \left(1 - \frac{\Delta t u_{i+1/2}^n}{h}\right) \rho_i^n + \frac{\Delta t u_{i+1/2}^n}{h} \rho_{i-1}^n, \quad (17)$$

which is a convex combination provided the CFL condition is satisfied

$$\Delta t < \frac{h}{\max_i(|u_{i+1/2}^n|)}. \quad (18)$$

It should be emphasised that this condition is far less stringent compared to that in Eq. (12) and does not depend on the density field. However, despite its intriguing positivity-preserving property, the upwind discretisation adds artificial dissipation to the equations, thus violating the FDB, as pointed out in Refs. [48,49]. On the other hand, the central reconstruction reproduces the FDB at the discrete level, while strongly limiting the timestep to ensure positivity. A way forward is a hybrid scheme combining the useful features of the two approaches while at the same time reducing their disadvantages. In principle, the upwind reconstruction is only required in the most rarefied regions, where a large timestep might lead to the occurrence of negative density values. A similar hybrid scheme was proposed in [49] but for simpler case of the overdamped version of the system in Eq. (2) where the momentum is slaved to the density.

We start by proposing a simple flux limiter:

$$\Phi(a, b) = \begin{cases} 0, & \min(a, b) < d \\ 1, & \min(a, b) \geq d, \end{cases} \quad (19)$$

where d plays the role of a threshold density value. With this definition, the hybrid reconstructed momentum reads

$$\hat{q}_{xi+1/2}^{HY} = \Phi(\rho_i, \rho_{i+1}) \hat{q}_{xi+1/2}^{CR} + (1 - \Phi(\rho_i, \rho_{i+1})) \hat{q}_{xi+1/2}^{UR}. \quad (20)$$

The basic idea is very simple: the flux limiter in Eq. (19) applies the central reconstruction when the densities in two neighbouring cells are both larger than the threshold value d , otherwise it enforces the upwind reconstruction. In the following section it will be shown that the proper choice of the threshold d can guarantee a minimum artificial dissipation, thus not drastically perturbing the FDB. We also illustrate the positivity preservation of the density with an affordable timestep via systematic numerical experiments.

The scheme is completed with the discretised version of the velocity equation. Here we adopted a centred approximation of all the derivatives, and centred interpolations of the fields where needed. In what follows we offer the explicit expression for the 1D case; the extension to the multidimensional case is straightforward. In 1D, the velocity equation reads

$$\rho \left(\frac{\partial u}{\partial t} + u \frac{\partial u}{\partial x} \right) = \frac{\partial}{\partial x} \left[-p - \frac{\lambda}{2} \left(\frac{\partial \rho}{\partial x} \right)^2 + \lambda \rho \frac{\partial^2 \rho}{\partial x^2} + \frac{4}{3} \mu \frac{\partial u}{\partial x} \right] + \frac{\partial}{\partial x} \left(\sqrt{2T\mu} W \right), \quad (21)$$

with W a normal distributed, delta-correlated in space and time, random field. The fully-discretised version, adopting the explicit forward Euler scheme, reads

$$\begin{aligned} \frac{u_{i+1/2}^{n+1} - u_{i+1/2}^n}{\Delta t} = & -\frac{u_{i+1/2}^n}{2h} (u_{i+3/2}^n - u_{i-1/2}^n) + \frac{1}{h\hat{\rho}_{i+1/2}^n} \left[-p(\rho_{i+1}^n) + p(\rho_i^n) - \frac{\lambda}{2(2h)^2} (\rho_{i+2}^n - \rho_i^n)^2 \right. \\ & + \frac{\lambda}{2(2h)^2} (\rho_{i+1}^n - \rho_{i-1}^n)^2 + \frac{\lambda \rho_{i+1}^n (\rho_{i+2}^n - 2\rho_{i+1}^n + \rho_i^n)}{h^2} - \frac{\lambda \rho_i^n (\rho_{i+1}^n - 2\rho_i^n + \rho_{i-1}^n)}{h^2} \left. \right] + \\ & + \frac{4\mu(\hat{\rho}_{i+1/2}^n)}{3h^2 \hat{\rho}_{i+1/2}^n} (u_{i+3/2}^n - 2u_{i+1/2}^n + u_{i-1/2}^n) + \frac{4}{3h\hat{\rho}_{i+1/2}^n} (\mu(\rho_{i+1}^n) - \mu(\rho_i^n)) \frac{u_{i+3/2}^n - u_{i-1/2}^n}{2h} \\ & + \frac{1}{h\hat{\rho}_{i+1/2}^n} \left(\sqrt{2T\mu(\rho_{i+1}^n)} W_{i+1}^n - \sqrt{2T\mu(\rho_i^n)} W_i^n \right), \end{aligned} \quad (22)$$

where $\hat{\rho}_{i+1/2}^n = (\rho_{i+1}^n + \rho_i^n)/2$. Finally, in Eq. (22), $\{W_i^n\}$ is a set of independent normal distributed random numbers, generated at each time step by appropriately transforming a set of uniformly distributed numbers extracted with the Marsenne twister algorithm [78].

It is noteworthy that we proved the positivity-preserving property for the upwinding scheme by adopting an explicit forward-Euler temporal integration. However, as discussed in Ref. [52], the property is also maintained with higher order Runge-Kutta schemes, as the solution is a convex combination of Euler substeps. In this work, all numerical simulations are performed with a second-order, Runge-Kutta method, RK2, that provides better stability and temporal accuracy with respect to the first-order Euler scheme.

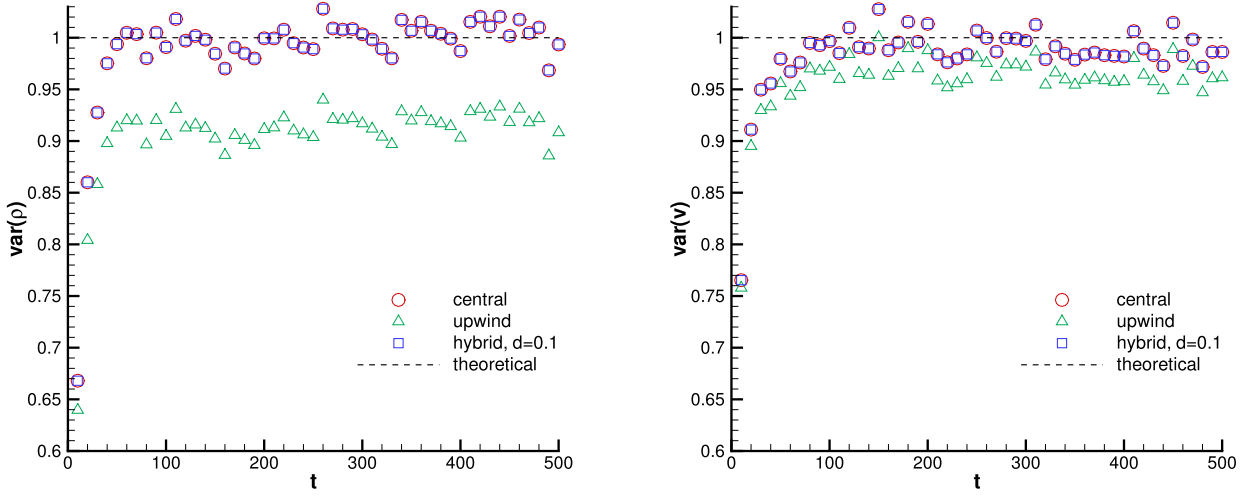


Fig. 1. Variance of the fluctuating fields with the different schemes in a liquid at $\langle \rho \rangle = 0.6$, $T = 1.2$. Left panel: variance of the density; Right panel: variance of the velocity. The values are normalised with the theoretical predictions.

4. Numerical applications

Here we provide tests of the hybrid numerical scheme developed in Sec. 3. More specifically, in subsection 4.1 we benchmark the equilibrium fluctuations in single-phase systems, liquid or vapour. In subsection 4.2 we compare the behaviour of the hybrid and of the fully-upwind schemes in reproducing the theoretical static structure factor of a capillary fluid described with the DI model. Subsection 4.3 is devoted to the analysis of thermal capillary waves at the liquid-vapour interface. Finally, in subsection 4.4 we assess the robustness of the proposed hybrid scheme with the numerical simulation of vapour-bubble nucleation. All numerical experiments are set in three-dimensional domains with periodic boundary conditions in all directions, with the exception of the simulations in subsec. 4.3 where a two-dimensional system is investigated.

4.1. Equilibrium fluctuations for a single-phase system

Analysis of fluctuations at equilibrium conditions is often used as a benchmark for the accuracy of numerical schemes in the context of FH modelling because theoretical predictions are available. In particular, for the case of a simple fluid without capillarity ($\lambda = 0$), the variance of the density and velocity fluctuations are compared with their theoretical counterparts

$$\langle \delta \rho^2 \rangle = \frac{T \langle \rho \rangle}{c_T^2 h^3}, \quad (23)$$

$$\langle \delta u^2 \rangle = \frac{T}{\langle \rho \rangle h^3}, \quad (24)$$

where $c_T^2 = (\partial p / \partial \rho)_T$ is the isothermal speed of sound to be evaluated at density $\langle \rho \rangle$ and temperature T . It is worth noting that the symbol, $\langle \cdot \rangle$, refers to the averaging operation against the probability-density function (PDF) of the fluctuating field. For example, the mean density is expressed as

$$\langle \rho \rangle = \int_{\text{supp}(\rho)} \rho P(\rho) d\rho, \quad (25)$$

where $\text{supp}(\rho)$ and $P(\rho)$ are the support and the PDF of the density field, respectively. In Fig. 1 we compare the fluctuations in a stable liquid at $\langle \rho \rangle = 0.6$, $T = 1.2$, using a grid size $h = 10$ and a timestep $\Delta t = 0.1$. In particular, the variance of the density field is numerically evaluated as

$$\text{var}(\rho) = \frac{1}{N} \sum_{i=1}^N (\rho_i - \langle \rho \rangle)^2, \quad (26)$$

with N the number of grid cells of the domain, relying on the statistical independency of the density values at the different locations. A similar expression is adopted to compute the numerical velocity variance. After a short transient, the variances reach a statistically stable value: the central scheme reproduces very well the expected variances, while the upwind scheme reveals a 10% error on the estimate of the density variance, and a smaller 3% error on the velocity variance. The hybrid

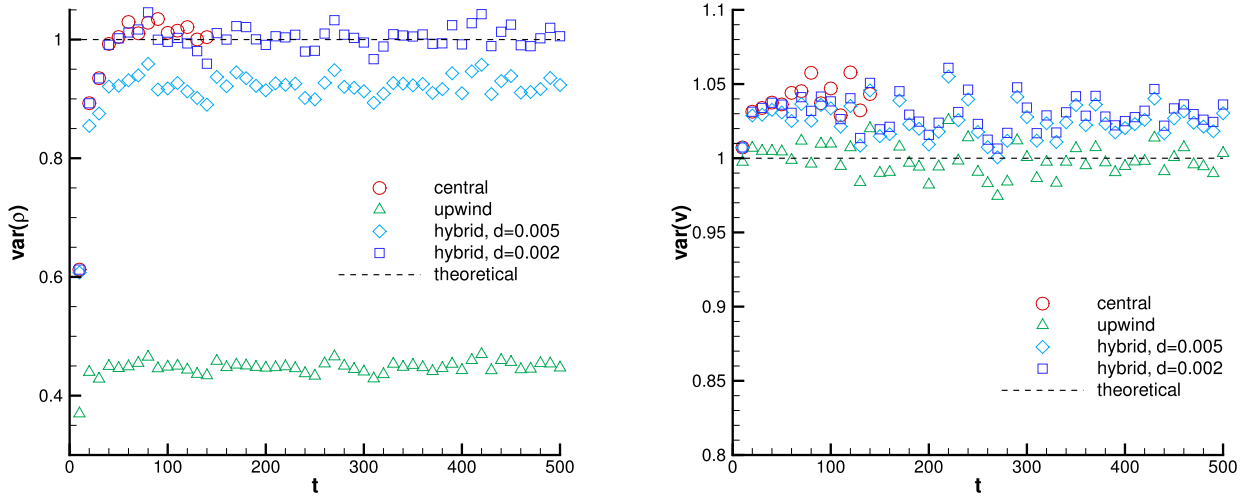


Fig. 2. Variance of the fluctuating fields with the different schemes in a vapour at $\langle \rho \rangle = 0.01$, $T = 1.2$. Left panel: variance of the density; Right panel: variance of the velocity. The values are normalised with the theoretical predictions. The data for the central scheme are interrupted at time $t = 140$ when a negative density is observed.

scheme, set up with a threshold $d = 0.1$ corresponding to the saturation vapour density at $T = 1.2$, reproduces very well the variances and totally overlaps the central scheme results. In fact in liquid conditions very few cells might cross the threshold, hence the low-order upwind reconstruction is practically never exploited.

A more stringent test is depicted in Fig. 2, where the equilibrium fluctuations in a rarefied vapour at $\langle \rho \rangle = 0.01$, $T = 1.2$ are analysed. Numerical integration is carried out by using $h = 11$ and a timestep $\Delta t = 0.1$. Again, after a short transient, the central scheme reaches the expected density variance. However, at time $t = 140$, and the specific sample shown in the figure, negative densities are encountered and the simulation blows out. This behaviour has been observed, at different times, in all the statistically independent samples we analysed, and occurred even when reducing the timestep to $\Delta t = 10^{-4}$. Instead, the upwind scheme is able to follow the dynamics for long times, but the measured variance of the density fluctuations is 55% smaller than the theoretical prediction.

Two different threshold values have been tested for the hybrid scheme. When using $d = 0.005$, corresponding to half the mean density, the error is only of the order of 10%; perfect agreement is obtained with $d = 0.002$ without the need of reducing the timestep. The velocity variance, on the right panel of Fig. 2, deserves a further comment. The theoretical value scales as $1/\langle \rho \rangle$ from Eq. (24), and reaches large values in rarefied vapour conditions, hence activating non-linear effects in the simulation. In these conditions the typical Landau-Lifshitz assumption of small fluctuations (i.e. $\sqrt{\langle \delta f^2 \rangle} / \langle f \rangle \ll 1$) is violated. As a consequence, the actual variances deviate from the expected theoretical values in Eq. (24) obtained through the linearised Landau-Lifshitz approach. In such cases the values of the variances obtained via FDB-compliant numerical simulations (central schemes) – fully taking into account any effect due to non-linearity – are more appropriate, and used here as the benchmark results instead of their theoretical counterpart. The hybrid scheme is then shown to be able to reproduce well the velocity variance with both threshold values we tested.

More detailed information concerning the statistical behaviour of the fluid fluctuations is provided by the PDFs. Gaussian distributions are expected for the cases where the typical fluctuations are smaller than the mean value: $\sqrt{\langle \delta g^2 \rangle} / \langle g \rangle \ll 1$, for the generic field g . In Figs. 3–4 the PDFs in liquid and vapour conditions, respectively, are reported and the behaviour of the different schemes is compared. Again, the hybrid scheme reproduces well the expected Gaussian distributions.

4.2. Static structure factor of a capillary fluid

The static structure factor (SSF) of the density field, $S_\rho(k) = \langle \delta \hat{\rho} \delta \hat{\rho}^* \rangle$, where $\delta \hat{\rho}$ represents the Fourier transform of the density fluctuations, is another benchmark for the numerical schemes developed for FH. In the case of simple fluids ($\lambda = 0$), a constant SSF is expected due to the spatial delta-correlation of the density fluctuations. A more interesting – and stringent test – is the case of capillary fluids, where the density-gradient term in the free-energy functional activates spatial density correlations. As a result, a non-homogeneous SSF is expected. A theoretical prediction is available:

$$S_\rho(k) = \frac{\langle \rho \rangle T}{c_T^2 + \lambda \langle \rho \rangle |\mathbf{k}|^2}, \quad (27)$$

with a $|\mathbf{k}|^{-2}$ decay at large wavenumbers in the Fourier space (a detailed derivation is provided in Appendix C).

Fig. 5 reports the case of a capillary fluid in a liquid state at the thermodynamic condition $T = 1.2$, $\langle \rho \rangle = 0.75$. The value of the nondimensional capillary coefficient is $\lambda^* = 5.2441$, and the simulation is performed with a uniform grid, $\Delta x = \Delta y =$

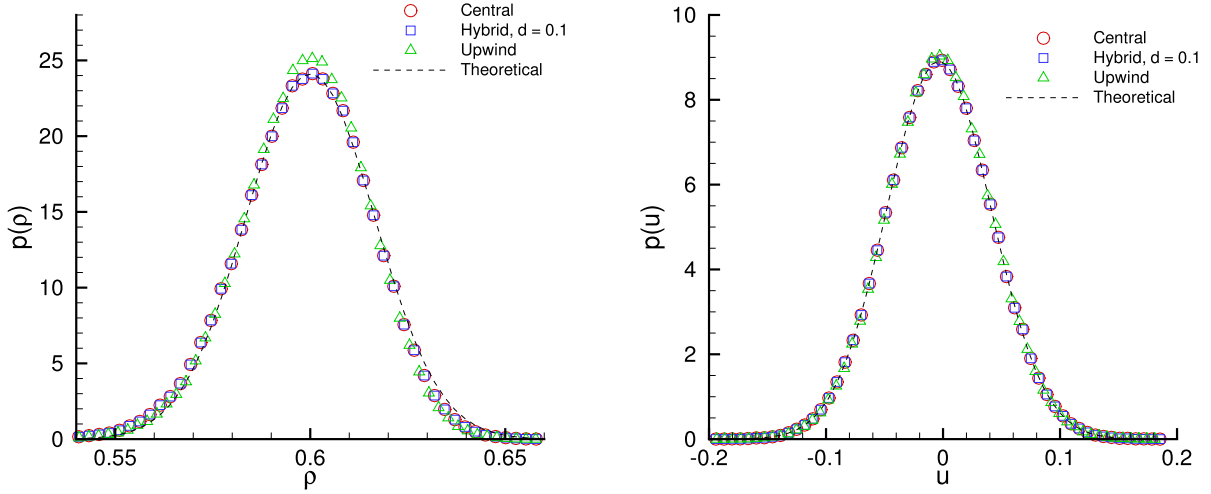


Fig. 3. PDFs, $P(\rho)$, of the density (left panel) and the velocity (right panel) fields, in the same conditions as reported in Fig. 1.

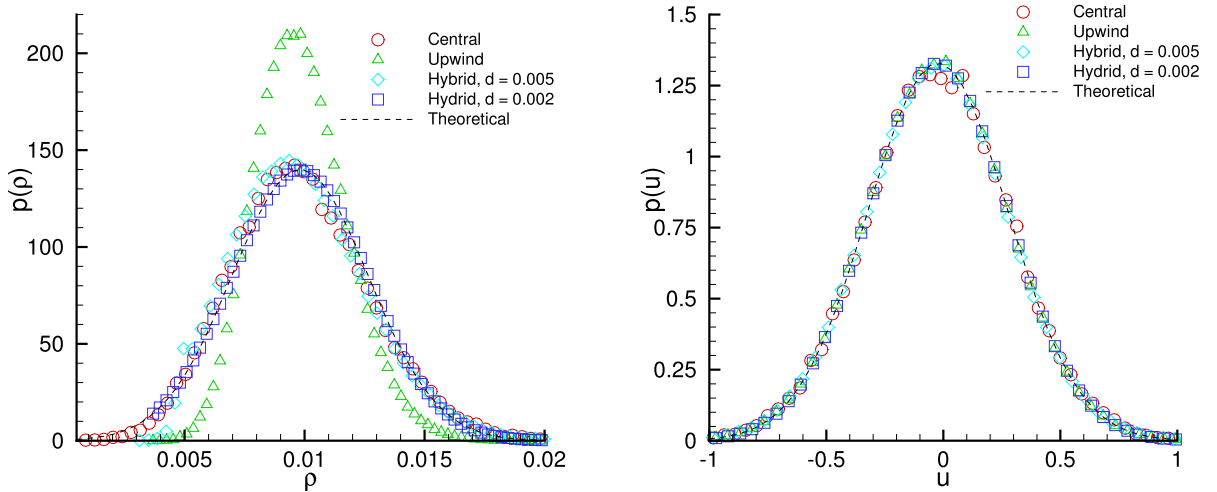


Fig. 4. PDFs, $P(\rho)$, of the density (left panel) and the velocity (right panel) fields, in the same conditions as reported in Fig. 2.

$\Delta z = 10$. The SSF has been numerically evaluated by averaging one million statistically independent samples amounting to a quite expensive simulation. The left panel of the figure shows a slice in the plane of wavenumbers k_x, k_y , comparing the results obtained with the hybrid (top half of the figure) and with the upwind (bottom half) schemes. There is a clear difference between the two schemes. A more quantitative comparison against the theoretical prediction, Eq. (27), is reported in the right panel of the figure, showing S_ρ as a function of $|\mathbf{k}|$. The hybrid scheme matches very well the theoretical expectation, especially at the largest wavenumbers. It is worthwhile noticing, however, that the statistical convergence of the smallest wavenumbers ($|\mathbf{k}| < 0.05$) would have required averaging over an even larger number of samples, because the largest fluid dynamics modes are characterised by slower convergence, in agreement with the literature [56].

To further evaluate the capabilities of our numerical scheme, we consider the case of a capillary fluid in a vapour state (at $T = 1.2$, $\langle \rho \rangle = 0.01$). The results are reported in Fig. 6. In stark contrast with the liquid case, here the SSF measured with the upwind scheme is completely altered by the additional numerical dissipation, producing a faster decay at large wavenumbers. On the contrary, the hybrid scheme set up with the threshold value $d = 0.002$, is very robust and able to reproduce the theoretical structure factor fairly well.

4.3. Thermal capillary waves

Thus far we verified the robustness of the hybrid scheme in reproducing the statistical properties of single phase systems. Here we turn our attention to thermal capillary waves, common phenomena in the realm of two-phase liquid-vapour systems. Such systems are well captured by DI modelling because it captures the effect of capillarity at the liquid-vapour interface. More precisely, we focus on the evaluation of the statistical properties of the equilibrium fluctuations of a liquid-

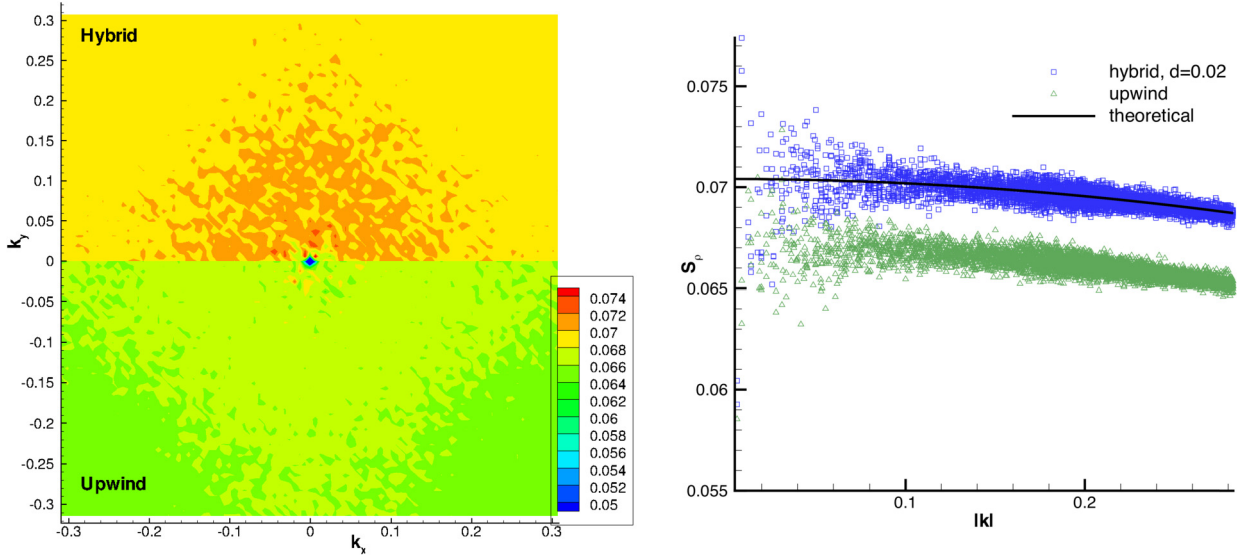


Fig. 5. SSF of the density fluctuations in a liquid at $T = 1.2$, $\langle \rho \rangle = 0.75$, $\lambda^* = 5.2441$, $\Delta x = \Delta y = \Delta z = 10$. The left panel compares the results, in the k_x - k_y plane, obtained with the hybrid (top half) and upwind (bottom half) schemes. The right panel plots the same data as a function of the wavenumber module $|\mathbf{k}|$ together with the theoretical prediction. (For interpretation of the colours in the figure(s), the reader is referred to the web version of this article.)

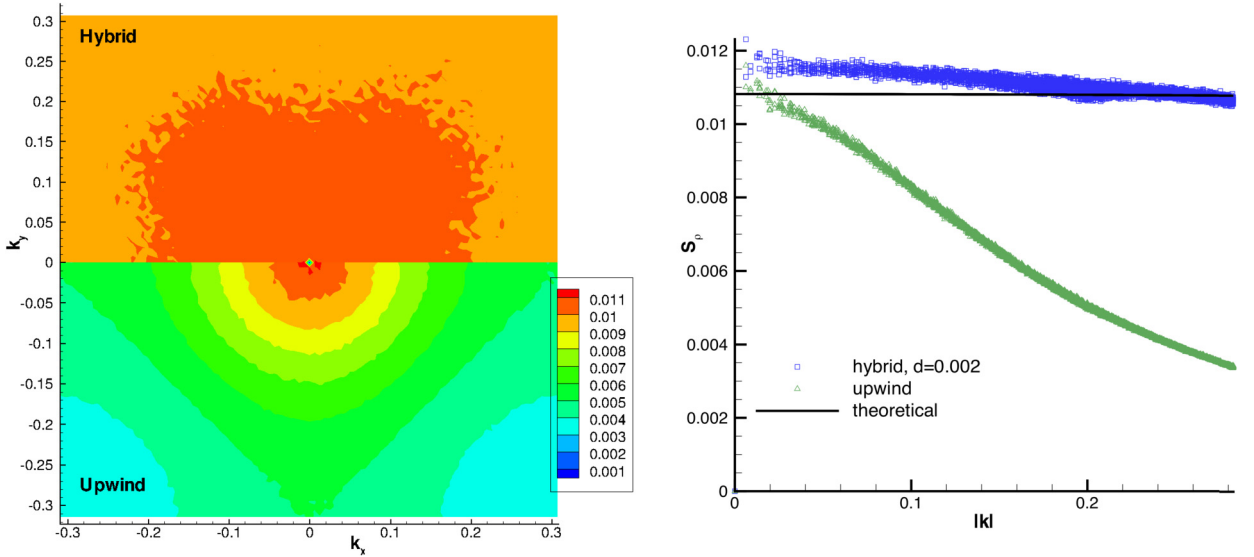


Fig. 6. SSF of the density fluctuations in a vapour at $T = 1.2$, $\langle \rho \rangle = 0.01$, $\lambda^* = 5.2441$, $\Delta x = \Delta y = \Delta z = 10$. The left panel compares the results in the k_x - k_y plane obtained with the hybrid (top half) and upwind (bottom half) schemes. The right panel plots the same data as a function of the wavenumber module $|\mathbf{k}|$ together with the theoretical prediction. (For interpretation of the colours in the figure(s), the reader is referred to the web version of this article.)

vapour interface. This is fundamental problem, and has been thoroughly analysed in terms of the statistical properties of the vertical displacement of the interface, $h(x)$ [14,79,80]. Capillary waves are in fact excited by thermal fluctuations and the spectrum of the interface displacement can be theoretically predicted from:

$$\langle |h(|\mathbf{k}|)|^2 \rangle = \frac{k_B T}{\sigma |\mathbf{k}|^2}, \quad (28)$$

where σ is the liquid-vapour surface tension (a complete derivation is given in Appendix C).

Here, we simulate a system with size $100 \times 100 \times 1$ using a grid size $\Delta x = \Delta y = \Delta z = 6$ and periodic boundary conditions, initialised with a slab of liquid at $T = 1.2$ in equilibrium with the vapour. The saturation densities at this temperature correspond to $\rho_L \simeq 0.567$, $\rho_V \simeq 0.1$. It is worth noticing that, in this two-phase case, liquid and vapour states are actually required to be at equilibrium. This indeed follows from the requirement of equal pressure (and chemical potential) in two phases separated by the statistically flat interface. As a consequence, the system is initialised with the two regions at

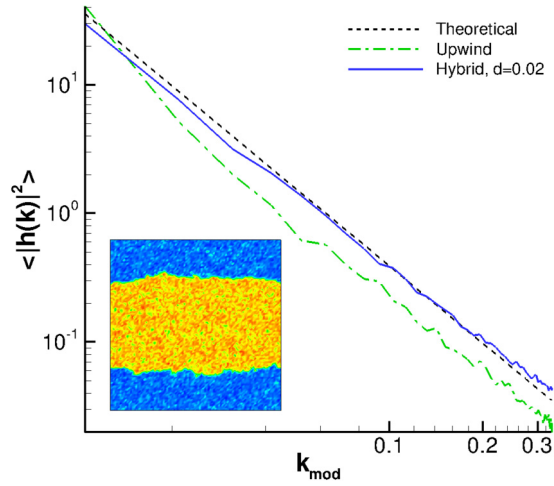


Fig. 7. The capillary wave spectrum, $\langle |h(k)|^2 \rangle$, obtained with the hybrid ($d = 0.02$) and the upwind schemes is compared with the theoretical prediction (dashed black line). The small inset shows one of the configurations of the system, with two corrugated liquid-vapour interfaces and the liquid slug almost at the centre.

the saturation liquid and vapour densities. In other words, we are not free to arbitrarily choose the density values in this case, as opposed to the previous sections where any stable vapour ($\rho < \rho_V$) or liquid ($\rho > \rho_L$) could be selected. The non-dimensional capillary coefficient is $\lambda^* = 5.244$. A set of 500 statistically independent samples, $\{h_s(x)\}$, is used to obtain the average spectra. The left panel of Fig. 7 shows the comparison of the capillary waves spectra obtained with the upwind and the hybrid schemes using the threshold value $d = 0.02$ for the hybrid scheme. The spectra are plotted as a function of the modified wave number $k_{mod} = \sin(k\Delta x/2)/(\Delta x/2)$ arising from the discretised version of the derivatives, as is commonly done in the literature [56]. In contrast with the hybrid scheme that perfectly reproduces the theoretical $|k|^{-2}$ scaling, the upwind scheme shows a faster decay due to the extra numerical dissipation, mostly impacting the largest wave numbers, hence smaller scales, as occurred with the SSF in the vapour system (§ 4.2).

4.4. Homogeneous bubble nucleation

So far we focused on the characterisation of statistical equilibrium properties. On the contrary, here we test our scheme against the homogeneous vapour bubble nucleation, a strongly out-of-equilibrium process. This problem is at the heart of our physical understanding of phase transition processes and liquid metastability [81], and not surprisingly it poses the strong need for an efficient and reliable numerical scheme. Previous attempts [17,57] have been limited to high temperatures, where the vapour density value is sufficiently high to reduce the possibility of blow-up in the simulations due to the occurrence of negative densities.

The full system of equations (10) is used, with the capillary coefficient $\lambda^* = 5.224$ that reproduces the surface tension value of the LJ fluid. The domain is initialised with a homogeneous metastable liquid at $\langle \rho \rangle = 0.51$, $T = 1.2$, while uniform grid with size $\Delta x = \Delta y = \Delta z = 10$ and a timestep $\Delta t = 0.1$ are used. Thermal fluctuations activate the phase transition and several vapour regions appear in the domain; only those larger than the critical size survive and expand further. There are two major quantities of interest: i) the nucleation rate, i.e. the number of bubbles formed per unit volume and unit time; ii) the expansion and coalescence bubble dynamics after the nucleation.

The time evolution of the number of vapour embryos, N_b , with a volume larger than three grid cells is reported in Fig. 8 depicting also the performance of the different schemes. Now there are no theoretical predictions and the central scheme results are used as benchmark. The time window with a linearly growing N_b is the one that characterises the so-called steady state nucleation, and allows to evaluate the nucleation rate as the slope of the curve $N_b(t)$ [82]. It is apparent that the hybrid scheme reproduces perfectly the slope of the central scheme, independently on the density threshold d . On the contrary, the upwind scheme reveals a delay in bubble formation and a smaller nucleation rate. It is also worth noting that the central scheme is not able to follow the entire dynamics, because the bubble growth leads to very small density values; fluctuations in the vapour regions, then, unavoidably produce negative densities and the blow-up of the simulation.

The analysis of the bubble growth dynamics is made possible by means of the hybrid and of the upwind schemes, due to the positivity-preserving property. During this stage, the dynamics is characterised by bubble expansion and coalescence, thus progressively reducing the number of bubbles in the domain. As is evident from the figure however, the choice of the density threshold d influences the results: simulations with the upwind scheme and with the hybrid one set-up with a large d value, show a faster decrease of the number of bubbles. This, however, is a numerical artefact due to the undesirable numerical diffusion artificially introduced by these schemes. As a matter of fact, when reducing d , we observe convergence of the solution, with the results unaffected by a further decrease below $d = 0.05$.

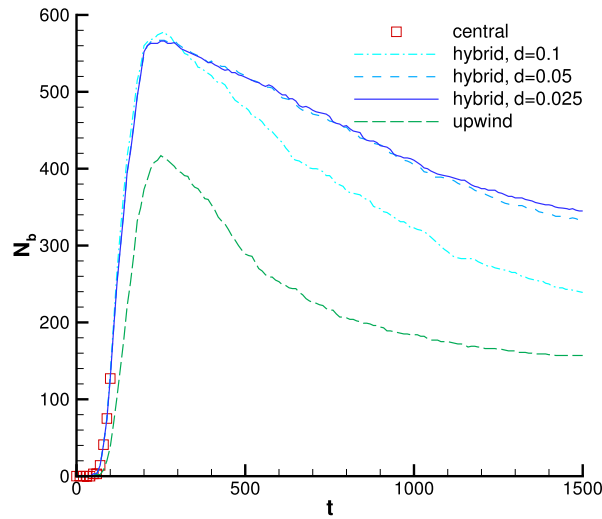


Fig. 8. Time evolution of the number of individual vapour bubbles nucleated in a metastable liquid at $\langle \rho \rangle = 0.51$, $T = 1.2$. The data for the central scheme are interrupted at time $t = 100$ when a negative density is encountered.

5. Conclusions and discussion

We have developed an accurate, efficient and robust numerical scheme for solving the FH equations in both single and two-phase systems, enabling to preserve in practice the positivity of the density. The scheme is based on a hybrid approach, applied to the convective term in the density equation of FH, combining a centred finite-difference discretisation on a uniform staggered grid with a first-order upwind scheme. The conservative reconstruction of the momentum is performed by applying a simple but efficient flux limiter Φ , which discriminates whether the centred scheme or the upwind one is utilised, according to the density values of the neighbouring cells. In particular, upwinding is deployed only where the density is lower than a prescribed threshold d . The hybrid scheme takes advantage of the central approximation adopted in most of the grid cells. Notwithstanding the introduction of local sources of numerical dissipation where the upwind is applied, the hybrid scheme is shown to be accurate, efficient and robust, capable to globally preserve the correct statistical properties of the fluctuating fields.

The scheme was validated with several case studies while also performing well-known benchmark tests. Both single and two-phase systems, equilibrium and out-of-equilibrium conditions, have been analysed. It was found that the threshold value d could be critical in reproducing the expected result. However, as a rule of thumb, a threshold $d \leq \rho_v/5$ (i.e. one fifth of the saturation vapour density in the case of two-phase flows, or one fifth of the initial vapour density in single-phase systems) reproduced the expected results in every single benchmark test. This value is sufficiently small not to introduce an appreciable amount of numerical dissipation, which in turn means that the scheme behaves globally as FDB-compliant, and – most importantly – warrants the positivity of the density without the need of reducing the timestep.

To further substantiate the practical validity of this empirical prescription, we performed a detailed convergence analysis investigating the density fluctuations in the low-density, stable vapour condition discussed in depth in Sec. 4.1. It is worthwhile to recall that a sound numerical convergence in stochastic equations should be understood in a statistical sense, i.e. weak convergence or convergence in probability. A common choice is to investigate convergence of the moments of the probability distribution, for example the second moment, i.e. the variance of the fluctuations. The FH theory provides a theoretical expected value for the density variance, Eq. (23), showing a scaling with the grid size as $\text{var}(\rho) \propto h^{-3}$. This is a common feature of SPDEs where intensive quantities diverge when the cell size shrinks to zero. As a matter of fact, the solution of SPDEs is intended in a distributional sense and as such it is not possible to achieve strong convergence with decreasing grid size. The physical interpretation is that the coarse graining procedure needed to derive the theory from the more fundamental atomistic model fails when the typical size of the coarse graining volume is of the order of the typical molecule size, the so-called “ultraviolet divergence” in statistical field theory [83].

Fig. 9 depicts the dependence of the density variance on the volume of the grid cell h^3 and on the threshold parameter d . The solid black line depicts the FH theoretical prediction, Eq. (23), and the curves with symbols correspond to different values of the parameter d . At high values of d (a condition where the upwind reconstruction is often recalled by our hybrid flux limiter, Eqs. (19), (20)), the disruption of the FDB leads to a wrong scaling law of the density variance. This occurs at d comparable with $\langle \rho \rangle$. Conversely, when d is reduced, we observe excellent agreement with the theoretical scaling h^{-3} , with a weak convergence of the solution for roughly $d < \langle \rho \rangle/5$. These findings substantiate the validity and reliability of the rule of thumb we have proposed.

We believe that the simplicity of our computational framework, combined with its ease of implementation and computational efficiency, will pave the way for its deployment to a wide spectrum of two-phase flows with large density ratios, such

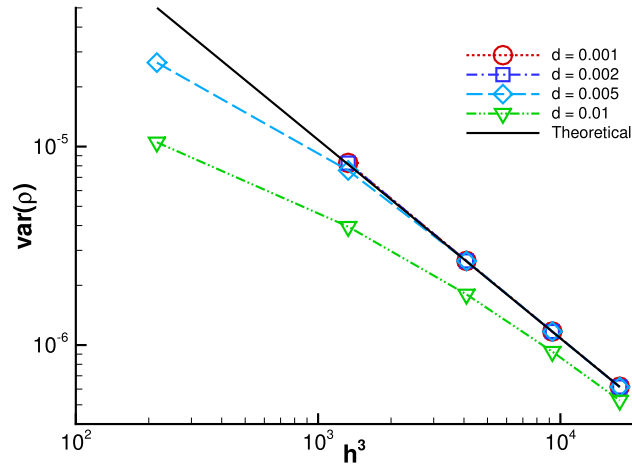


Fig. 9. Variance of the density fluctuations in the low-density, stable-vapour condition discussed in Sec. 4.1, as a function of the volume of the numerical grid cell. The solid black line represents the FH theoretical prediction. The other curves report the behaviour of our hybrid scheme at different values of the threshold parameter d as per legend. Excellent agreement with the theoretical scaling is obtained with $d = 0.002 = \langle \rho \rangle / 5$.

as the liquid-vapour phase transitions at low temperatures which commonly lead to numerical instabilities. Of particular interest would also be extension of the scheme to non-isothermal cases, where the temperature field must remain positive, but also multi-component systems where the concentration is another positive quantity.

CRediT authorship contribution statement

Francesco Magaletti: Conceptualization, Investigation, Methodology, Software, Visualization, Writing – original draft. **Mirko Gallo:** Formal analysis, Investigation, Methodology, Visualization, Writing – original draft. **Sergio P. Perez:** Methodology, Writing – review & editing. **José A. Carrillo:** Methodology, Supervision, Writing – review & editing. **Serafim Kalliadasis:** Methodology, Supervision, Writing – review & editing.

Declaration of competing interest

The authors declare that they have no known competing financial interests or personal relationships that could have appeared to influence the work reported in this paper.

Acknowledgements

We gratefully acknowledge DECI (WETONB project) resource EAGLE hosted by PSNC (Poland), and the DECI (SOLID project Deci 17) resource Navigator Cluster based in Portugal at www.uc.pt/lca/ClusterResources/Navigator, with support from the PRACE aisbl, where the computations reported here were performed. F.M. was supported by the European Union's Horizon 2020 Programme under the Marie Skłodowska-Curie via Grant No. [836693]. The work of M.G. was supported by Sapienza through the project ASSEMBLE. J.A.C. was supported by the ERC Advanced Grant Nonlocal-CPD (Nonlocal PDEs for Complex Particle Dynamics: Phase Transitions, Patterns and Synchronization) under the European Union's Horizon 2020 Programme, Grant No. 883363), and the Engineering and Physical Sciences Research Council of the UK via Grants No. EP/T022132/1 and EP/V051121/1. S.P.P. acknowledges financial support from the Imperial College President's PhD Scholarship scheme.

Appendix A. Derivation of the Korteweg stress tensor

Here we retrace the derivation of the Korteweg stress tensor for an isothermal capillary fluid. The adopted procedure is framed in the context of non-equilibrium thermodynamics [35], and it has been exploited to derive the structure of thermodynamic fluxes in non-isothermal conditions [69], where the specific form of the thermodynamic fluxes is obtained by enforcing a positive entropy production (Clausius-Duhem inequality). Similarly, for an isothermal system, thermodynamically consistent constitutive relations for the stress tensor can be derived by imposing that the total free energy, the Hamiltonian of the system, $\mathcal{H} = F + K$, must be a decreasing function of time, with F and K the Helmholtz and kinetic energies, respectively.

In the present case, the Hamiltonian reads:

$$\mathcal{H}[\rho, \mathbf{u}] = \int_V \rho \left(f(\rho, T) + \frac{\lambda}{2\rho} |\nabla \rho|^2 + \frac{1}{2} \mathbf{u} \cdot \mathbf{u} \right) dV. \quad (\text{A.1})$$

The irreversible nature of viscous fluid motion enforces

$$\frac{d\mathcal{H}}{dt} = \int_V \rho \frac{D\eta}{Dt} dV \leq 0, \quad (\text{A.2})$$

where $\eta = f(\rho, T) + \lambda/2\rho|\nabla\rho|^2 + \frac{1}{2}\mathbf{u} \cdot \mathbf{u}$ is the Hamiltonian density per unit mass, $D/Dt = \partial/\partial t + \mathbf{u} \cdot \nabla$ is the material derivative operator, and T is the temperature. To obtain an evolution equation for η we express the density and momentum equations in non-conservative form,

$$\begin{aligned} \frac{D\rho}{Dt} &= -\rho \nabla \cdot \mathbf{u}, \\ \rho \frac{D\mathbf{u}}{Dt} &= \nabla \cdot \boldsymbol{\tau}, \end{aligned} \quad (\text{A.3})$$

so that,

$$\frac{D\eta}{Dt} = \frac{\partial\eta}{\partial\rho} \frac{D\rho}{Dt} + \frac{\partial\eta}{\partial\nabla\rho} \cdot \frac{D\nabla\rho}{Dt} + \frac{\partial\eta}{\partial\mathbf{u}} \cdot \frac{D\mathbf{u}}{Dt}. \quad (\text{A.4})$$

By substituting Eqs. (A.3) in the equation above and after some simple algebra, the entropy evolution equation reads

$$\rho \frac{D\eta}{Dt} = \frac{1}{\rho} \left(p_0 - \frac{\lambda}{2} |\nabla\rho|^2 \right) \frac{D\rho}{Dt} + \lambda \nabla\rho \cdot \frac{D\nabla\rho}{Dt} + \mathbf{u} \cdot \nabla \cdot \boldsymbol{\tau}, \quad (\text{A.5})$$

with the pressure $p_0 = \rho^2(\partial f/\partial\rho)_T$. To close the equation, the evolution of the density gradient is required. This can be evaluated by applying the gradient operator to Eq. (A.3) leading to

$$\frac{D\nabla\rho}{Dt} = -\nabla\rho \cdot \nabla \otimes \mathbf{u} - \nabla(\rho \nabla \cdot \mathbf{u}). \quad (\text{A.6})$$

As a result,

$$\rho \frac{D\eta}{Dt} = \left(-p_0 + \frac{\lambda}{2} |\nabla\rho|^2 \right) \nabla \cdot \mathbf{u} - \lambda \nabla\rho \cdot \nabla(\rho \nabla \cdot \mathbf{u}) - \lambda \nabla\rho \otimes \nabla\rho : \nabla \otimes \mathbf{u} - \mathbf{u} \cdot \nabla \cdot \boldsymbol{\tau}, \quad (\text{A.7})$$

and the time derivative of the Hamiltonian can be written as

$$\frac{d\mathcal{H}}{dt} = \int_V \left[\left(-p_0 + \frac{\lambda}{2} |\nabla\rho|^2 + \lambda\rho \nabla^2\rho \right) \mathbf{I} - \lambda \nabla\rho \otimes \nabla\rho - \boldsymbol{\tau} \right] : \nabla \otimes \mathbf{u} dV, \quad (\text{A.8})$$

where integration by parts has been applied on the second and last terms of the right-hand-side of Eq. (A.7).

The stress tensor $\boldsymbol{\tau}$ can now be decomposed in two distinct parts, $\boldsymbol{\tau}_{rev}$ that does not dissipate energy, and $\boldsymbol{\tau}_{irr}$ corresponding to viscous dissipation. The two contributions can then be identified as

$$\boldsymbol{\tau}_{rev} = \left(-p_0 + \frac{\lambda}{2} |\nabla\rho|^2 + \lambda\rho \nabla^2\rho \right) \mathbf{I} - \lambda \nabla\rho \otimes \nabla\rho, \quad (\text{A.9})$$

the Korteweg stress tensor, and the usual viscous stress

$$\boldsymbol{\tau}_{irr} = \mu \left(\nabla \otimes \mathbf{u} + \nabla \otimes \mathbf{u}^T - \frac{2}{3} \nabla \cdot \mathbf{u} \mathbf{I} \right). \quad (\text{A.10})$$

Introducing the symmetric part of the velocity gradient, $\mathbf{E} = (\nabla \otimes \mathbf{u} + \nabla \otimes \mathbf{u}^T)/2$, it is straightforward to verify that the Hamiltonian evolution is a decreasing function of time,

$$\frac{d\mathcal{H}}{dt} = -2\mu \int_V \mathbf{E}_{dev} : \mathbf{E}_{dev} dV \leq 0, \quad (\text{A.11})$$

with $\mathbf{E}_{dev} = \mathbf{E} - 1/3 \nabla \cdot \mathbf{u} \mathbf{I}$ the deviatoric part of the tensor \mathbf{E} .

Appendix B. Static correlation function of the fluctuating fields

The static correlation function (SSF) of a thermodynamic system in equilibrium with constant temperature T , given mass M and fixed volume V , can be evaluated from the deviation of the Hamiltonian, $\Delta\mathcal{H}$, from its equilibrium value, \mathcal{H}_0 . For the single component system at equilibrium density ρ_0 , and equilibrium velocity $\mathbf{u}_0 = \mathbf{0}$, $\Delta\mathcal{H}$ can be expressed as

$$\Delta\mathcal{H}[\rho, \mathbf{u}] = \mathcal{H} - \mathcal{H}_0 = \Delta\mathcal{H}[\rho, \mathbf{v}] = \int_V \rho f(\rho, T) + \frac{\lambda}{2} |\nabla \rho|^2 + \frac{1}{2} \rho \mathbf{u} \cdot \mathbf{u} - \rho f(\rho_0, T) dV, \quad (\text{B.1})$$

The probability distribution functional of the fluctuating fields $\Delta = (\rho, \mathbf{u}) - (\rho_0, \mathbf{0}) = (\delta\rho, \delta\mathbf{u})$ follows from Einstein's stipulation,

$$P_{eq}[\Delta] = \frac{1}{Z} \exp(-\beta \Delta\mathcal{H}), \quad (\text{B.2})$$

with $\beta = 1/(k_B T)$. The SSF can be thus evaluated by solving the path integral

$$\mathbf{C}_\Delta(\mathbf{x}) = \langle \Delta \otimes \Delta^\dagger \rangle = \frac{1}{Z} \int D\Delta \Delta \otimes \Delta^\dagger \exp(-\beta \Delta\mathcal{H}). \quad (\text{B.3})$$

Assuming that the fluid is close to equilibrium, and the fluctuations are small with respect to the mean value, the Hamiltonian deviation, $\Delta\mathcal{H}$, can be approximated by a quadratic form in the fluctuating fields:

$$\Delta\mathcal{H} \simeq \frac{1}{2} \int_V \left(\frac{c_{T0}^2}{\rho_0} \delta\rho^2 - \lambda \delta\rho \nabla^2 \delta\rho + \rho_0 \delta\mathbf{u} \cdot \delta\mathbf{u} \right) dV, \quad (\text{B.4})$$

where $c_{T0}^2 = \partial p_0 / \partial \rho|_T(\rho_0, T)$. This allows to approximate the actual non-Gaussian PDF (B.2) as

$$P_{eq}[\Delta] = \frac{1}{Z} \exp \left(-\frac{1}{2} \beta \int_V \Delta^\top \mathbf{H} \Delta dV \right), \quad (\text{B.5})$$

where \mathbf{H} is a diagonal positive-definite matrix, whose entries are

$$H_{\delta\rho\delta\rho} = \frac{c_{T0}^2}{\rho_0} - \lambda \nabla^2 \quad (\text{B.6})$$

$$H_{\delta\mathbf{u}\delta\mathbf{u}} = \rho_0 \mathbf{I} \quad (\text{B.7})$$

with \mathbf{I} the 2×2 identity matrix. The above PDF can be factorised as follows,

$$P_{eq}[\Delta] = P_{\delta\rho}[\delta\rho] P_{\delta\mathbf{u}}[\delta\mathbf{u}], \quad (\text{B.8})$$

with

$$P_{\delta\rho}[\delta\rho] = \frac{1}{Z_{\delta\rho}} \exp \left(-\frac{1}{2} \beta \int_V \int_{V'} dV dV' \delta\rho(\mathbf{r}) H_{\delta\rho\delta\rho} \delta(\mathbf{r} - \mathbf{r}') \delta\rho(\mathbf{r}') \right),$$

$$P_{\delta\mathbf{u}}[\delta\mathbf{u}] = \frac{1}{Z_{\delta\mathbf{u}}} \exp \left(-\frac{1}{2} \beta \int_V \int_{V'} dV dV' \delta\mathbf{u}^\top(\mathbf{r}) H_{\delta\mathbf{u}\delta\mathbf{u}} \delta(\mathbf{r} - \mathbf{r}') \delta\mathbf{u}(\mathbf{r}') \right), \quad (\text{B.9})$$

and with the normalization constant Z

$$Z = \int D\delta\rho D\delta\mathbf{u} \exp \left(-\frac{1}{2} \beta \int_V \Delta^\top \mathbf{H} \Delta dV \right) = Z_{\delta\rho} Z_{\delta\mathbf{u}}. \quad (\text{B.10})$$

The correlation tensor (B.3) can be evaluated in closed form by integrating Gaussian path integrals. For this calculation it is instrumental to introduce the characteristic functional of the stochastic process. Given the PDF, $P[x]$, of a generic stochastic scalar process $x(\mathbf{r})$, the characteristic functional reads:

$$\Phi[\lambda] = \int Dx P[x] \exp \left(\int \lambda(\mathbf{r}') x(\mathbf{r}') d\mathbf{r}' \right). \quad (\text{B.11})$$

When considering the PDF of a Gaussian process

$$P[x] = \exp\left(\int -\frac{1}{2}x(\mathbf{r})A(\mathbf{r}, \mathbf{r}')x(\mathbf{r}')d\mathbf{r}d\mathbf{r}'\right),$$

the characteristic functional reduces to

$$\Phi[\lambda] = \int D\lambda \exp\left(-\frac{1}{2} \iint d\mathbf{r}d\mathbf{r}' x(\mathbf{r}) A(\mathbf{r}, \mathbf{r}') x(\mathbf{r}') + \int \lambda(\mathbf{r}) x(\mathbf{r}) d\mathbf{r}\right) \quad (\text{B.12})$$

that can be evaluated by completing the square as

$$\Phi[\lambda] = \Phi[0] \exp\left(\frac{1}{2} \iint d\mathbf{r}d\mathbf{r}' \lambda(\mathbf{r}) G(\mathbf{r}, \mathbf{r}') \lambda(\mathbf{r}')\right), \quad (\text{B.13})$$

where

$$G(\mathbf{r}, \mathbf{r}') = A^{-1}(\mathbf{r}, \mathbf{r}'). \quad (\text{B.14})$$

The two-point correlation is then written as

$$C_{xx}(\mathbf{r}, \mathbf{r}') = \langle x(\mathbf{r}) x(\mathbf{r}') \rangle = \left(\frac{1}{\Phi[0]} \frac{\delta}{\delta \lambda(\mathbf{r}')} \frac{\delta}{\delta \lambda(\mathbf{r})} \Phi[\lambda] \right)_{\lambda=0} = G(\mathbf{r}, \mathbf{r}'). \quad (\text{B.15})$$

In the present multicomponent case the kernel of the operator \mathbf{A} is given by

$$\mathbf{A}(\mathbf{r}, \mathbf{r}') = \beta \mathbf{H} \delta(\mathbf{r} - \mathbf{r}'), \quad (\text{B.16})$$

implying that

$$\int \mathbf{A}(\mathbf{r}, \mathbf{r}'') \mathbf{G}(\mathbf{r}'', \mathbf{r}') d\mathbf{r}'' = \beta \int \mathbf{H} \delta(\mathbf{r} - \mathbf{r}'') \mathbf{G}(\mathbf{r}'', \mathbf{r}') d\mathbf{r}'' = \delta(\mathbf{r} - \mathbf{r}'). \quad (\text{B.17})$$

In particular, since the matrix \mathbf{H} is diagonal, the $\delta\rho\delta\rho$ component of the above equation is

$$\int A_{\delta\rho\delta\rho}(\mathbf{r}, \mathbf{r}'') G_{\delta\rho\delta\rho}(\mathbf{r}'', \mathbf{r}') d\mathbf{r}'' = \beta \int H_{\delta\rho\delta\rho} \delta(\mathbf{r} - \mathbf{r}'') G_{\delta\rho\delta\rho}(\mathbf{r}'', \mathbf{r}') d\mathbf{r}'' = \delta(\mathbf{r} - \mathbf{r}'), \quad (\text{B.18})$$

where the Dirac delta function on the right hand side is, clearly, the kernel of the identity operator. Given the expression of $H_{\delta\rho\delta\rho}$, Eq. (B.6), the solution of Eq. (B.18) for $G_{\delta\rho\delta\rho}$ satisfies:

$$\left(\frac{c_T^2}{\rho_0} - \lambda \nabla_{\mathbf{r}}^2 \right) G_{\delta\rho\delta\rho}(\mathbf{r}, \mathbf{r}') = \frac{1}{\beta} \delta(\mathbf{r} - \mathbf{r}'). \quad (\text{B.19})$$

The solution of Eq. (B.19) is readily obtained by means of the Fourier transforms

$$\delta(\mathbf{r} - \mathbf{r}') = \int_{-\infty}^{+\infty} \exp[-j\mathbf{k} \cdot (\mathbf{r} - \mathbf{r}')] d\mathbf{k}, \quad (\text{B.20})$$

$$G_{\delta\rho\delta\rho}(\mathbf{r} - \mathbf{r}') = \int_{-\infty}^{+\infty} \hat{G}_{\delta\rho\delta\rho}(\mathbf{k}) \exp[-j\mathbf{k} \cdot (\mathbf{r} - \mathbf{r}')] d\mathbf{k}, \quad (\text{B.21})$$

Therefore, the Green function $G_{\delta\rho\delta\rho}$ is easily evaluated in the Fourier space as,

$$\hat{G}_{\delta\rho\delta\rho}(\mathbf{k}) = \frac{k_B T \rho_0}{c_T^2 + \lambda \mathbf{k} \cdot \mathbf{k}}. \quad (\text{B.22})$$

The same procedure is used on the velocity component of the correlation tensor. After some algebra, the correlation tensor $\hat{\mathbf{C}}_{\mathbf{A}}$ in Fourier space is given as follows:

$$\hat{\mathbf{C}}_{\mathbf{A}}(\mathbf{k}) = \hat{\mathbf{C}}_{\mathbf{A}}(\mathbf{k}) = \begin{pmatrix} \frac{k_B T \rho_0}{c_T^2 + \lambda \mathbf{k} \cdot \mathbf{k}} & 0 \\ 0 & \frac{k_B T}{\rho_0} \mathbf{I} \end{pmatrix}. \quad (\text{B.23})$$

It is worth noticing that, in the Gaussian approximation, the velocity equilibrium correlations are delta-correlated in the physical space, while capillarity induces a correlation length in the density fluctuations. Finally, the cross-correlation of the fluctuating fields vanishes.

Appendix C. Thermal fluctuations of liquid-vapour interfaces

As discussed in the previous Appendix, the SSF of a physical system is connected to the free energy of the system. In particular the probability of observing a specific system configuration is related exponentially to the free-energy deviation from the equilibrium value. Here we will describe the capillary-wave spectrum of a “statistically”-flat liquid-vapour interface. For that purpose we adopt a prototypical system consisting of a sharp (zero thickness) interface separating the liquid from its vapour phase. The interface can be described as a two-dimensional manifold Σ immersed in a three-dimensional space \mathbb{R}^3 , whose Helmholtz free energy

$$F[\Sigma] = \sigma \int_{\Sigma} dS \quad (C.1)$$

represents the Hamiltonian of the system, with σ the surface tension. To describe the fluctuating shape of the interface, it is useful to introduce the Monge representation of the manifold Σ through the height function $h(x, y) : A \subset \mathbb{R}^2 \rightarrow \mathbb{R}$, so that $dS = \sqrt{1 + \nabla h \cdot \nabla h}$, where $\nabla = (\partial/\partial x, \partial/\partial y)$. Under this particular parametrisation, the free-energy functional in Eq. (C.1) takes the form

$$F[h] = \sigma \int_A \sqrt{1 + \nabla h \cdot \nabla h} da, \quad (C.2)$$

with $da = dx dy$. For a statistically-flat interface, i.e. $\langle h \rangle = h_0$, the height function h can be decomposed as $h = h_0 + h'$. In addition, under the hypothesis of small undulations with respect to the interface extension, $h' \ll \sqrt{\text{mis}(A)}$, the functional in Eq. (C.2) can be expanded as:

$$F[h'] = \sigma \int_A \left(1 + \frac{1}{2} |\nabla h'|^2 \right) da. \quad (C.3)$$

Then the free-energy deviation from the equilibrium value, $F_0 = \sigma \text{mis}(A)$, is given from:

$$\Delta F[h'] = \frac{1}{2} \sigma \int_A |\nabla h'|^2 da = -\frac{1}{2} \sigma \int_A h' \nabla^2 h' da, \quad (C.4)$$

and the PDF of the interface fluctuation becomes:

$$P_{eq}[h'] = \frac{1}{Z} \exp(-\beta \Delta F[h']). \quad (C.5)$$

Equation (C.5) represents a Gaussian probability distribution whose correlation function reads (details are given in Appendix B)

$$\langle h'(\mathbf{a}) h'(\mathbf{a}') \rangle = \frac{1}{Z} \int D h' h'(\mathbf{a}) h'(\mathbf{a}') \exp \left(-\frac{1}{2} \int_A \int_{A'} da da' h'(\mathbf{a}) \Gamma(\mathbf{a}, \mathbf{a}') h'(\mathbf{a}') \right) = \Gamma^{-1}(\mathbf{a}, \mathbf{a}'), \quad (C.6)$$

with $\mathbf{a} \in A$ a generic position in A and $\Gamma(\mathbf{a}, \mathbf{a}') = -\sigma \beta \nabla^2 \delta(\mathbf{a} - \mathbf{a}')$. To evaluate the inverse of Γ , i.e. the interface height correlation, we follow the same procedure adopted in Appendix B (see Eq. (B.18)) which yields:

$$\int \Gamma(\mathbf{a}, \mathbf{a}'') G_{hh}(\mathbf{a}'', \mathbf{a}') da'' = \delta(\mathbf{a} - \mathbf{a}'), \quad (C.7)$$

This is equivalent to identifying the Green function as

$$-\sigma \beta \nabla^2 G_{hh}(\mathbf{a}, \mathbf{a}') = \delta(\mathbf{a} - \mathbf{a}'), \quad (C.8)$$

which can be directly determined by applying the Fourier transform on both sides, leading to,

$$G_{hh}(\mathbf{k}) = \langle h(\mathbf{k}) h(-\mathbf{k}) \rangle = \frac{k_B T}{\sigma |\mathbf{k}|^2}. \quad (C.9)$$

References

- [1] M. Gallo, F. Magaletti, C.M. Casciola, Heterogeneous bubble nucleation dynamics, *J. Fluid Mech.* 906 (2021).
- [2] J.F. Lutsko, How crystals form: a theory of nucleation pathways, *Sci. Adv.* 5 (2019) eaav7399.
- [3] M.A. Durán-Olivencia, R.S. Gvalani, S. Kalliadasis, G.A. Pavliotis, Instability, rupture and fluctuations in thin liquid films: theory and computations, *J. Stat. Phys.* 174 (2019) 579–604.
- [4] C. Zhao, D.A. Lockerby, J.E. Sprittles, Dynamics of liquid nanothreads: fluctuation-driven instability and rupture, *Phys. Rev. Fluids* 5 (2020) 044201.
- [5] F. Detcheverry, L. Bocquet, Thermal fluctuations in nanofluidic transport, *Phys. Rev. Lett.* 109 (2012) 024501.
- [6] A. Naji, P.J. Atzberger, F.L. Brown, Hybrid elastic and discrete-particle approach to biomembrane dynamics with application to the mobility of curved integral membrane proteins, *Phys. Rev. Lett.* 102 (2009) 138102.
- [7] C.S. Peskin, G.M. Odell, G.F. Oster, Cellular motions and thermal fluctuations: the Brownian ratchet, *Biophys. J.* 65 (1993) 316.
- [8] A. Russo, M.A. Durán-Olivencia, S. Kalliadasis, R. Hartkamp, Macroscopic relations for microscopic properties at the interface between solid substrates and dense fluids, *J. Chem. Phys.* 150 (2019) 214705.
- [9] S. Marchio, S. Meloni, A. Giacomello, C. Valeriani, C. Casciola, Pressure control in interfacial systems: atomistic simulations of vapor nucleation, *J. Chem. Phys.* 148 (2018) 064706.
- [10] L. Landau, E. Lifshitz, *Statistical Physics, Course of Theoretical Physics*, vol. 5, 1980, p. 30.
- [11] P.J. Atzberger, P.R. Kramer, C.S. Peskin, A stochastic immersed boundary method for fluid-structure dynamics at microscopic length scales, *J. Comput. Phys.* 224 (2007) 1255–1292.
- [12] K. Lazaridis, L. Wickham, N. Voulgarakis, Fluctuating hydrodynamics for ionic liquids, *Phys. Lett. A* 381 (2017) 1431–1438.
- [13] M. Moseler, U. Landman, Formation, stability, and breakup of nanojets, *Science* 289 (2000) 1165–1169.
- [14] B.Z. Shang, N.K. Voulgarakis, J.-W. Chu, Fluctuating hydrodynamics for multiscale simulation of inhomogeneous fluids: mapping all-atom molecular dynamics to capillary waves, *J. Chem. Phys.* 135 (2011) 044111.
- [15] A. Donev, T.G. Fai, E. Vanden-Eijnden, A reversible mesoscopic model of diffusion in liquids: from giant fluctuations to Fick's law, *J. Stat. Mech. Theory Exp.* 2014 (2014) P04004.
- [16] M. Gallo, F. Magaletti, D. Cocco, C.M. Casciola, Nucleation and growth dynamics of vapour bubbles, *J. Fluid Mech.* 883 (2020).
- [17] M. Gallo, F. Magaletti, C.M. Casciola, Fluctuating hydrodynamics as a tool to investigate nucleation of cavitation bubbles, *Int. J. Comput. Methods Exp. Meas.* 6 (2017) 345–357.
- [18] F. Magaletti, A. Georgoulas, M. Marengo, Unraveling low nucleation temperatures in pool boiling through fluctuating hydrodynamics simulations, *Int. J. Multiph. Flow* 130 (2020) 103356.
- [19] K. Kawasaki, Stochastic model of slow dynamics in supercooled liquids and dense colloidal suspensions, *Physica A* 208 (1994) 35–64.
- [20] D.S. Dean, Langevin equation for the density of a system of interacting Langevin processes, *J. Phys. A, Math. Gen.* 29 (1996) L613.
- [21] J.F. Lutsko, A dynamical theory of nucleation for colloids and macromolecules, *J. Chem. Phys.* 136 (2012) 034509.
- [22] C. Cornalba, T. Shardlow, J. Zimmer, A regularized Dean-Kawasaki model: derivation and analysis, *SIAM J. Math. Anal.* 51 (2019) 1137–1187.
- [23] H. Wensik, H. Löwen, Aggregation of self-propelled colloidal rods near confining walls, *Phys. Rev. E* 78 (2008) 031409.
- [24] Particle-scale statistical theory for hydrodynamically induced polar ordering in microswimmer suspensions, *J. Chem. Phys.* 149 (2018) 144902.
- [25] Y.-X. Yu, J. Wu, Density functional theory for inhomogeneous mixtures of polymeric fluids, *J. Chem. Phys.* 117 (2002) 2368–2376.
- [26] J. Wu, Density functional theory for chemical engineering: from capillarity to soft materials, *AIChE J.* 52 (2006) 1169–1193.
- [27] B.D. Goddard, A. Nold, N. Savva, G.A. Pavliotis, S. Kalliadasis, General dynamical density functional theory for classical fluids, *Phys. Rev. Lett.* 109 (2012) 120603.
- [28] B.D. Goddard, G.A. Pavliotis, S. Kalliadasis, The overdamped limit of dynamic density functional theory: rigorous results, *SIAM Multiscale Model. Simul.* 10 (2012) 633–663.
- [29] M.A. Durán-Olivencia, B.D. Goddard, S. Kalliadasis, Dynamical density functional theory for orientable colloids including inertia and hydrodynamic interactions, *J. Stat. Phys.* 164 (2016) 785–809.
- [30] J.A. Carrillo, S. Kalliadasis, S.P. Perez, C.-W. Shu, Well-balanced finite-volume schemes for hydrodynamic equations with general free energy, *SIAM Multiscale Model. Simul.* 18 (2020) 502–541.
- [31] M. te Vrugt, H. Löwen, R. Wittkowski, Classical dynamical density functional theory: from fundamentals to applications, *Adv. Phys.* 69 (2020) 121–247.
- [32] M.A. Durán-Olivencia, P. Yatsyshin, B.D. Goddard, S. Kalliadasis, General framework for fluctuating dynamic density functional theory, *New J. Phys.* 19 (2017) 123022.
- [33] R.F. Fox, G.E. Uhlenbeck, Contributions to non-equilibrium thermodynamics. I. Theory of hydrodynamical fluctuations, *Phys. Fluids* (1958–1988) 13 (1970) 1893–1902.
- [34] J.M.O. De Zarate, J.V. Sengers, *Hydrodynamic Fluctuations in Fluids and Fluid Mixtures*, Elsevier, 2006.
- [35] D.S. Dean, Groot, P. Mazur, *Non-equilibrium Thermodynamics*, Courier Dover Publications, 2013.
- [36] A.J. Archer, Dynamical density functional theory for molecular and colloidal fluids: a microscopic approach to fluid mechanics, *J. Chem. Phys.* 130 (2009) 014509.
- [37] B.D. Goddard, A. Nold, N. Savva, P. Yatsyshin, S. Kalliadasis, Unification of dynamic density functional theory for colloidal fluids to include inertia and hydrodynamic interactions: derivation and numerical experiments, *J. Phys.: Condens. Matter* 25 (2013) 035101.
- [38] P. Español, H.C. Öttinger, On the interpretation of random forces derived by projection operators, *Z. Phys. B, Condens. Matter* 90 (1993) 377–385.
- [39] H. Grabert, Fokker-Planck equation approach to fluctuations about nonequilibrium steady states, *J. Stat. Phys.* 26 (1981) 113–135.
- [40] W. Van Saarloos, D. Bedeaux, P. Mazur, Non-linear hydrodynamic fluctuations around equilibrium, *Phys. A, Stat. Mech. Appl.* 110 (1982) 147–170.
- [41] D. Zubarev, V. Morozov, Statistical mechanics of nonlinear hydrodynamic fluctuations, *Phys. A, Stat. Mech. Appl.* 120 (1983) 411–467.
- [42] P. Español, Stochastic differential equations for non-linear hydrodynamics, *Phys. A, Stat. Mech. Appl.* 248 (1998) 77–96.
- [43] A. Donev, E. Vanden-Eijnden, A. Garcia, J. Bell, On the accuracy of finite-volume schemes for fluctuating hydrodynamics, *Commun. Appl. Math. Comput. Sci.* 5 (2010) 149–197.
- [44] A. Donev, A. Nonaka, Y. Sun, T. Fai, A. Garcia, J. Bell, Low Mach number fluctuating hydrodynamics of diffusively mixing fluids, *Commun. Appl. Math. Comput. Sci.* 9 (2014) 47–105.
- [45] F. Balboa, J.B. Bell, R. Delgado-Buscalioni, A. Donev, T.G. Fai, B.E. Griffith, C.S. Peskin, Staggered schemes for fluctuating hydrodynamics, *SIAM Multiscale Model. Simul.* 10 (2012) 1369–1408.
- [46] P. Español, A. Donev, Coupling a nano-particle with isothermal fluctuating hydrodynamics: coarse-graining from microscopic to mesoscopic dynamics, *J. Chem. Phys.* 143 (2015) 234104.
- [47] J. De La Torre, P. Español, A. Donev, Finite element discretization of non-linear diffusion equations with thermal fluctuations, *J. Chem. Phys.* 142 (2015) 094115.
- [48] S. Delong, B.E. Griffith, E. Vanden-Eijnden, A. Donev, Temporal integrators for fluctuating hydrodynamics, *Phys. Rev. E* 87 (2013) 033302.
- [49] A. Russo, S.P. Perez, M.A. Durán-Olivencia, P. Yatsyshin, J.A. Carrillo, S. Kalliadasis, A finite-volume method for fluctuating dynamical density functional theory, *J. Comput. Phys.* 428 (2021) 109796.

- [50] B. Einfeldt, C.-D. Munz, P.L. Roe, B. Sjögreen, On Godunov-type methods near low densities, *J. Comput. Phys.* 92 (1991) 273–295.
- [51] H.-Z. Tang, K. Xu, Positivity-preserving analysis of explicit and implicit Lax–Friedrichs schemes for compressible Euler equations, *J. Sci. Comput.* 15 (2000) 19–28.
- [52] X. Zhang, C.-W. Shu, On positivity-preserving high order discontinuous Galerkin schemes for compressible Euler equations on rectangular meshes, *J. Comput. Phys.* 229 (2010) 8918–8934.
- [53] X. Zhang, Y. Xia, C.-W. Shu, Maximum-principle-satisfying and positivity-preserving high order discontinuous Galerkin schemes for conservation laws on triangular meshes, *J. Sci. Comput.* 50 (2012) 29–62.
- [54] X. Zhang, C.-W. Shu, Positivity-preserving high order finite difference weno schemes for compressible Euler equations, *J. Comput. Phys.* 231 (2012) 2245–2258.
- [55] X. Zhang, On positivity-preserving high order discontinuous Galerkin schemes for compressible Navier–Stokes equations, *J. Comput. Phys.* 328 (2017) 301–343.
- [56] A. Chaudhri, J.B. Bell, A.L. Garcia, A. Donev, Modeling multiphase flow using fluctuating hydrodynamics, *Phys. Rev. E* 90 (2014) 033014.
- [57] M. Gallo, F. Magaletti, C.M. Casciola, Thermally activated vapor bubble nucleation: the Landau–Lifshitz–van der Waals approach, *Phys. Rev. Fluids* 3 (2018) 053604.
- [58] R. Evans, The nature of the liquid–vapour interface and other topics in the statistical mechanics of non-uniform, classical fluids, *Adv. Phys.* 28 (1979) 143–200.
- [59] P. Yatsyshin, N. Savva, S. Kalliadasis, Geometry-induced phase transitions in fluids: Capillary prewetting, *Phys. Rev. E* 87 (2013), 020402(R).
- [60] P. Yatsyshin, N. Savva, S. Kalliadasis, Wetting of prototypical one- and two-dimensional systems: Thermodynamics and density functional theory, *J. Chem. Phys.* 142 (2015) 034708.
- [61] P. Yatsyshin, N. Savva, S. Kalliadasis, Density functional study of condensation in capped capillaries, *J. Phys.: Condens. Matter.* 27 (2015) 275104.
- [62] P. Yatsyshin, A.O. Parry, C. Rascón, S. Kalliadasis, Wetting of a plane with a narrow solvophobic stripe, *Mol. Phys.* 116 (2018) 1990–1997.
- [63] P. Yatsyshin, S. Kalliadasis, Surface nanodrops and nanobubbles: a classical density functional theory study, *J. Fluid Mech.* 913 (2021) A45.
- [64] J.F. Lutsko, Density functional theory of inhomogeneous liquids. IV. Squared-gradient approximation and classical nucleation theory, *J. Chem. Phys.* 134 (2011) 164501.
- [65] A. Pereira, S. Kalliadasis, Equilibrium gas–liquid–solid contact angle from density-functional theory, *J. Fluid Mech.* 692 (2012) 53–77.
- [66] H.C. Öttinger, M. Grmela, Dynamics and thermodynamics of complex fluids. II. Illustrations of a general formalism, *Phys. Rev. E* 56 (1997) 6633.
- [67] P. Espanol, Thermohydrodynamics for a van der Waals fluid, *J. Chem. Phys.* 115 (2001) 5392–5403.
- [68] F. Magaletti, L. Marino, C. Casciola, Shock wave formation in the collapse of a vapor nanobubble, *Phys. Rev. Lett.* 114 (2015) 064501.
- [69] F. Magaletti, M. Gallo, L. Marino, C.M. Casciola, Shock-induced collapse of a vapor nanobubble near solid boundaries, *Int. J. Multiph. Flow* 84 (2016) 34–45.
- [70] F. Magaletti, M. Gallo, L. Marino, C.M. Casciola, Dynamics of a Vapor Nanobubble Collapsing Near a Solid Boundary, *Journal of Physics: Conference Series*, vol. 656, IOP Publishing, 2015, p. 012012.
- [71] R. Teshigawara, A. Onuki, Spreading with evaporation and condensation in one-component fluids, *Phys. Rev. E* 82 (2010) 021603.
- [72] C. Wylock, M. Pradas, B. Haut, P. Colinet, S. Kalliadasis, Disorder-induced hysteresis and nonlocality of contact line motion in chemically heterogeneous microchannels, *Phys. Fluids* 24 (2012) 032108.
- [73] T. Laurila, A. Carlson, M. Do-Quang, T. Ala-Nissila, G. Amberg, Thermohydrodynamics of boiling in a van der Waals fluid, *Phys. Rev. E* 85 (2012) 026320.
- [74] J.K. Johnson, J.A. Zollweg, K.E. Gubbins, The Lennard-Jones equation of state revisited, *Mol. Phys.* 78 (1993) 591–618.
- [75] R. Rowley, M. Painter, Diffusion and viscosity equations of state for a Lennard-Jones fluid obtained from molecular dynamics simulations, *Int. J. Thermophys.* 18 (1997) 1109–1121.
- [76] J.A. Carrillo, A. Chertock, Y. Huang, A finite-volume method for nonlinear nonlocal equations with a gradient flow structure, *Commun. Comput. Phys.* 17 (2015) 233–258.
- [77] R. Bailo, J.A. Carrillo, S. Kalliadasis, S.P. Perez, Unconditional bound-preserving and energy-dissipating finite-volume schemes for the Cahn–Hilliard equation, *arXiv preprint, arXiv:2105.05351*, 2021.
- [78] M. Matsumoto, T. Nishimura, Mersenne twister: a 623-dimensionally equidistributed uniform pseudo-random number generator, *ACM Trans. Model. Comput. Simul. (TOMACS)* 8 (1998) 3–30.
- [79] J.S. Rowlinson, B. Widom, *Molecular Theory of Capillarity*, Courier Corporation, 2013.
- [80] A.-L. Barabási, H. Stanley, *Fractal Concepts in Surface Growth*, Cambridge University Press, 1995.
- [81] Q. Zheng, D. Durben, G. Wolf, C. Angell, Liquids at large negative pressures: water at the homogeneous nucleation limit, *Science* 254 (1991) 829–832.
- [82] J. Diemand, R. Angélik, K.K. Tanaka, H. Tanaka, Large scale molecular dynamics simulations of homogeneous nucleation, *J. Chem. Phys.* 139 (2013) 074309.
- [83] G. Lythe, S. Habib, Stochastic pdes: convergence to the continuum?, *Comput. Phys. Commun.* 142 (2001) 29–35.